Polarization lidar operation for measuring backscatter phase matrices of oriented scatterers

Matthew Hayman,[1,*] **Scott Spuler,**[2] **Bruce Morley**[2] **and Joseph VanAndel**[2]

[1]*National Center for Atmospheric Research, Advanced Study Program, Boulder, CO, 80307, USA*

[2]*National Center for Atmospheric Research, Earth Observing Lab, Boulder, CO, 80307, USA*

**mhayman@ucar.edu*

Abstract: We describe implementation and demonstration of a polarization technique adapted for lidar to measure all unique elements of the volume backscatter phase matrix. This capability allows for detection of preferential orientation within a scattering volume, and may improve scattering inversions on oriented ice crystals. The technique is enabled using a Mueller formalism commonly employed in polarimetry, which does not require the lidar instrument be polarization preserving. Instead, the accuracy of the polarization measurements are limited by the accuracy of the instrument characterization. A high spectral resolution lidar at the National Center for Atmospheric Research was modified to demonstrate this polarization technique. Two observations where the instrument is tilted off zenith are presented. In the first case, the lidar detects flattened large raindrops oriented along the same direction due to drag forces from falling. The second case is an ice cloud approximately 5 km above lidar base that contains preferentially oriented ice crystals in a narrow altitude band.

OCIS codes: (010.3640) Lidar; (010.1615) Clouds; (120.5410) Polarimetry.

References and links

1. T. A. Seliga and V. N. Bringi, "Potential use of radar differential reflectivity measurements at orthogonal polarizations for measuring precipitation," J. Appl. Meteor. **15**, 69–76 (1976).
2. J. Vivekanandan, G. Zhang, and E. Brandes, "Polarimetric radar estimators based on a constrained gamma drop size distribution model," J. Appl. Meteor. **43**, 217–230 (2004).
3. R. Greenler, *Rainbows, Halos, and Glories* (Cambridge U. Press, 1980).
4. Y. Tanko and K. Liou, "Solar radiative transfer in cirrus clouds. Part II: Theory and computation of multiple scattering in an anisotropic medium," J. Atmos. Sci. **46**, 20–36 (1989).
5. A. Heymsfield and J. Iaquinta, "Cirrus crystal terminal velocity," J. Atmos. Sci. **57**, 916–938 (2000).
6. C. D. Westbrook, "The fall speeds of sub-100μm ice crystals," Q. J. R. Meteorol. Soc. **134**, 1243–1251 (2008).
7. V. Noel and K. Sassen, "Study of planar ice crystal orientation in ice clouds from scanning polarization lidar observations," J. Appl. Meteor. **44**, 653–664 (2005).
8. V. Noel and H. Chepfer, "Study of ice crystal orientation in cirrus clouds based on satellite polarized radiance measurements," J. Atmos. Sci. **61**, 2073–2081 (2005).
9. K. Masuda and H. Ishimoto, "Influence of particle orientation on retrieving cirrus cloud properties by use of total and polarized reflectances from satellite measurements," J. Quant. Spectrosc. Radiat. Transfer **85**, 183–193 (2004).
10. M. Hayman and J. P. Thayer, "General description of polarization in lidar using Stokes vectors and polar decomposition of Mueller matrices," J. Opt. Soc. Am. A **29**, 400–409 (2012).

#179024 - $15.00 USD Received 30 Oct 2012; revised 6 Dec 2012; accepted 6 Dec 2012; published 19 Dec 2012

11. Y. Balin, B. Kaul, G. Kokhanenko, and D. Winker, "Application of circularly polarized laser radiation for sensing of crystal clouds," Opt. Express **17**, 6849–6859 (2009).
12. C. M. R. Platt, "Lidar backscatter from horizontal ice crystal plates," J. Appl. Meteorol. **17**, 482-488 (1978).
13. L. Thomas, J. C. Cartwright, and D. P. Wareing, "Lidar observations of the horizontal orientation of ice crystals in cirrus clouds," Tellus B **42**, 2011–2016 (1990).
14. S. A. Young, C. M. R. Platt, R. T. Austin, and G. R. Patterson, "Optical properties and phase of some midlatitude, midlevel clouds in ECLIPS," J. Appl. Meteorol. **39**, 135–153 (2000).
15. Y. Hu, P. Yang, B. Lin, G. Gibson, and C. Hostetler, "Discriminating between spherical and non-spherical scatterers," J. Quant. Spectrosc. Radiat. Transfer **79-80**, 757–764 (2004).
16. C. Zhou, P. Yang, A. E. Dessler, Y. Hu, and B. A. Baum, "Study of horizontally oriented ice crystals with CALIPSO observations and comparision with monte carlo radiative transfer simulations," J. Appl. Meteor. Climatol. **51**, 1426–1439 (2012).
17. W. H. Hunt, D. M. Winker, M. A. Vaughan, K. A. Powell, P. L. Lucker, and C. Weimer, "CALIPSO lidar description and performance assessment," J. Atmos. Oceanic Technol. **26**, 1214–1228 (2009).
18. C. D. Westbrook, A. J. Illingworth, E. J. O'Connor, and R. J. Hogan, "Doppler lidar measurements of oriented planar ice crystals falling from supercooled and glaciated layer clouds," Q. J. R. Meteor. Soc. **136**, 260–276 (2010).
19. F-M Bréon and B. Dubrulle, "Horizontally oriented plates in clouds," J. Atmos. Sci. **61**, 2888–2898 (2004).
20. A. J. Heymsfield and M. Kajikawa, "An improved approach to calculating terminal velocities of plate-like crystals and graupel," J. Atmos. Sci. **44**, 1088–1099 (1987).
21. M. D. Gusta, E. Vallar, O. Riviere, F. Castagnoli, V. Venturi, and M. Morandi, "Use of polarimetric lidar for the study of oriented ice plates in clouds," Appl. Opt. **45**, 4878-4887 (2006).
22. M. D. Shupe, D. D. Turner, V. P. Walden, R. Bennartz, M. P. Cadeddu, B. B. Castellani, C. J. Cox, D. R. Hudak, M. S. Kulie, N. B. Miller, R. R. Neely, and W. D Neff, "High and dry: New observations of tropospheric and cloud properties above the Greenland Ice Sheet," B. Am. Meteorol. Soc. doi:10.1175/BAMS-D-11-00249, In Press.
23. R. R. Neely, M. Hayman, R. Stillwell, J. P. Thayer, R. M. Hardesty, M. O'Neill, M. D. Shupe, and C. Alvarez, "Polarization lidar at Summit, Greenland for the detection of cloud phase and particle orientation," J. Atmos. Oceanic Technol. In Review.
24. B. V. Kaul, I. V. Samokhvalov, and S. N. Volkov, "Investigating particle orientation in cirrus clouds by measuring backscattering phase matrices with lidar," Appl. Opt. **43**, 6620–6628 (2004).
25. J. S. Tyo, Z. Wang, S. J. Johnson, and B. G. Hoover, "Design and optimization of partial Mueller matrix polarimeters," Appl. Opt. **49**, 2326–2332 (2010).
26. K. M. Twietmeyer, and R. A. Chipman, "Optimization of Mueller matrix polarimeters in the presence of error sources," Opt. Express **16**, 11589–11603 (2008).
27. M. H. Smith, "Optimization of a duel-rotating-retarder Mueller matrix polarimeter," Appl. Opt. **41** 2488-2493 (2002).
28. E. Eloranta, Chapter 5: High Spectral Resolution Lidar in *Lidar: Range-Resolved Optical Remote Sensing of the Atmosphere* New York, U.S.A. (Springer, 2005).
29. P. Piironen and E. Eloranta, "Deomonstration of a high-spectral-resolution lidar based on an iodine absorption filter," Opt. Lett. **19**, 234–236 (1994).
30. G. G. Matvienko, I. V. Samokhvalov, and B. V. Kaul, "Research of the cirrus structure with a polarization lidar: parameters of particle orientation in crystal clouds," in Proc. SPIE **5571**, 393–400 (2004).
31. H. van de Hulst, *Light Scattering by Small Particles* (Wiley, 1981).
32. M. Mishchenko and J. Hovenier, "Depolarization of light backscattered by randomly oriented nonspherical particles," Opt. Lett. **20**, 1356–1358 (1995).
33. C. J. Flynn, A. Mendoza, Y. Zheng, and S. Mathur, "Novel polarization-sensitive micropulse lidar measurement technique," Opt. Express **15**, 2785–2790 (2007).
34. G. Gimmestad, "Reexamination of depolarization in lidar measurements," Appl. Opt. **47**, 3795–3802 (2008).
35. M. Mishchenko, J. W. Hovenier, and L. D. Travis, *Light Scattering by Nonspherical Particles*, (Academic, 2000).
36. S. M. Kay, *Fundamentals of Statistical Signal Processing, **I**: Estimation Theory*, (Prentice Hall, 1993).
37. M. Hayman and J. Thayer, "Lidar polarization measurements of PMCs," J. Atmos. Sol. Terr. Phys. **73**, 2110–2117 (2011).
38. A. Zardecki and A. Deepak, "Forward multiple scattering corrections as a function of detector field of view," Appl. Opt. **22**, 2970–2976 (1983).
39. X. Zhu, "Explicit Jones transformation matrix for a tilted birefringent plate with its optic axis parallel to the plate surface," Appl. Opt. **33**, 3502–3506 (1994).
40. S. C. McClain, L. W. Hillman, and R. A. Chipman, "Polarization ray tracing in anisotropic optically active media. I. Algorithms," J. Opt. Soc. Am. A **10**, 2371–2382 (1993).
41. S. C. McClain, L. W. Hillman, and R. A. Chipman, "Polarization ray tracing in anisotropic optically active media. II. Theory and physics," J. Opt. Soc. Am. A **10**, 2383–2393 (1993).

#179024 - $15.00 USD Received 30 Oct 2012; revised 6 Dec 2012; accepted 6 Dec 2012; published 19 Dec 2012

1. Introduction

Interpretation of polarization lidar data generally assumes that the scattering volume consists of randomly oriented particles. This assumption, however, is invalid in some cases. Large raindrops deform from perfect spheroids due to drag; resulting in what is approximated as horizontally oriented oblate spheroids [1, 2]. Ice crystals also orient under certain conditions which sometimes result in optical phenomena such as sun dogs, pillars and arcs [3].

It has been suggested that ice crystal orientation may have an impact on radiative transfer through increased cloud albedo [4] and cloud lifetime through fall speed [5, 6]. In [7] it was suggested that horizontal orientation is the natural state of ice crystals in the atmosphere and [8] estimated that 40% of all high clouds observed by the Polarization and Directionality of Earth Reflectances (POLDER) satellite mission contained oriented ice crystals. Still, it is not clear if oriented ice crystals occur in sufficient concentration and frequency to significantly impact Earth's radiation budget.

The occurrence of preferential orientation also presents an issue when interpreting remote sensing data. Satellite retrievals of ice cloud optical depth and particle shape can vary significantly depending on the assumed orientation of the scatterers [9]. Furthermore, polarization parameters retrieved by lidar systems can have ambiguous meaning when oriented ice crystals are present [10, 11]. The core problem is that measurement methods capable of detecting preferential orientation are rarely employed.

Horizontally oriented plates are often identified by directing a lidar along zenith or nadir. The presence of horizontally oriented plates will result in observation of a high backscatter, low depolarization specular reflection [12–16]. CALIPSO used this technique for a 17 month period, but was subsequently tilted off nadir, because the specular signals tend to overwhelm other cloud and aerosol observations [17]. Scanning capability was used in [7] to allow for better characterization of the orientation distribution and randomly oriented ice crystal properties.

Specular reflections produce robust signatures of oriented plates, but they generally cannot contribute additional information about the oriented crystals (i.e. habit, size, etc.). In one instance, however, a Doppler lidar was used to determine the fall speed of the oriented crystals [18]. Using microphysical growth and aerodynamic properties of plates, the ice crystal size and shape could then be inferred [19, 20].

Off-zenith polarization measurements present a means for detecting and characterizing ice crystals through their unique polarization signatures without sacrificing other cloud and aerosol data. In [21], the backscatter Stokes vector was measured to detect the presence of oriented ice crystals and the Cloud Aerosol Backscatter and Depolarization Lidar (CAPABL) measures backscatter phase matrix diattenuation, a polarization effect only attributable to oriented scatterers [22, 23].

By measuring the full backscatter phase matrix, all polarization properties of an arbitrary scattering volume may be characterized. Such a measurement of oriented ice crystals provides five unique polarization parameters, which would likely improve scattering inversions of the oriented population. However, to our knowledge, this measurement has only performed by [24]. Perhaps this is because the design, hardware, and processing complexity commonly thought to be necessary for such a measurement create a practical deterrent. However, through the use of a vectorized Mueller matrix formalism that is commonly employed in polarimetry [25–27], we have developed a simple methodology for measuring the full backscattered matrix. The method does not require a highly polarization preserving instrument or elaborate polarization hardware. Its accuracy is defined by the accuracy of instrument characterization, which is necessary to process the data for scattering matrix retrieval. Through the use of a single rotating quarter wave-plate (QWP), we modified the high spectral resolution lidar (HSRL) at the National Center for Atmospheric Research (NCAR) to measure the full backscatter phase matrix without

#179024 - $15.00 USD Received 30 Oct 2012; revised 6 Dec 2012; accepted 6 Dec 2012; published 19 Dec 2012

loss of conventional HSRL data products [28,29]. We will describe the methodology employed in this measurement and system characterization and show observations of scattering matrices for rain and an ice cloud containing oriented ice crystals.

2. Theory

The end-to-end relationship from laser to measured optical signal is given by the Stokes Vector Lidar Equation (SVLE) where polarization states are represented as Stokes vectors and each term along the optical path is a Mueller matrix [10]. The equation is written

$$N(R) = \vec{o}^T \mathbf{M_{RX}} \left[\left(G(R) \frac{A}{R^2} \Delta R \right) \mathbf{T_{atm}}(\vec{k}_s, R) \mathbf{F}(\vec{k}_i, \vec{k}_s, R) \mathbf{T_{atm}}(\vec{k}_i, R) \mathbf{M_{TX}} \vec{S}_{TX} + \vec{S}_B \right], \quad (1)$$

where N is the signal recorded on the detector, $\vec{S}_{TX}$ is the Stokes vector describing the laser polarization state, $\mathbf{M_{TX}}$ is the Mueller matrix description of the transmitter and includes the polarization state generator, $\mathbf{T_{atm}}(\vec{k}_i, R)$ is the Mueller matrix description of the atmospheric transmission to the scatterer along incident wave vector $\vec{k}_i$ over the range R, $\mathbf{F}(\vec{k}_i, \vec{k}_s, R)$ is the scattering phase matrix (or Mueller matrix) of the scattering medium at range R for incident and scattered wave vectors $\vec{k}_i$ and $\vec{k}_s$ respectively, ΔR is the integration range bin, A is the collection aperture, $G(R)$ is the geometrical overlap function, $\mathbf{M_{RX}}$ is the Mueller matrix description of the receiver which, for polarization lidar, contains a polarization analyzer, and $\vec{S}_B$ is the Stokes vector of the background at the input of the receiver. Finally, $\vec{o}^T$ is the 1×4 output vector representing the fact that only the first element of the Stokes vector is measured by the optical detector and is written

$$\vec{o}^T = \begin{bmatrix} \eta & 0 & 0 & 0 \end{bmatrix}, \quad (2)$$

where η is the detector efficiency. In this work, all vectors are column vectors. Row vectors have the superscript ^{T}, denoting a transpose operation.

In the case of polarization measurements, atmospheric extinction is not expected to have a significant impact on the transmitted polarization state [15, 30] so the scattering matrix $\mathbf{F}(\vec{k}_i, \vec{k}_s, R)$ is the only polarization term in the SVLE that contains information about the atmosphere. However, additional terms in the instrument matrices generally present an issue necessitating correction to produce an accurate characterization of the atmosphere.

The polarization properties of the backscatter phase matrix can be used to distinguish randomly oriented and preferentially oriented scatterers. In cases where the volume consists of randomly oriented particles, the backscatter phase matrix takes the form [31–34]

$$\mathbf{F}(\pi) = \beta \begin{bmatrix} 1 & 0 & 0 & f_{14} \\ 0 & 1-d & 0 & 0 \\ 0 & 0 & d-1 & 0 \\ f_{14} & 0 & 0 & 2d-1 \end{bmatrix}, \quad (3)$$

where β is the volume backscatter coefficient and d is the "propensity of the medium to depolarize." In cases of randomly oriented scatterers, the medium is macroscopically isotropic, so direction of incidence is dropped from the backscatter phase matrix argument.

The backscatter phase matrix for preferentially oriented scatterers is distinctively different, exhibiting all three polarization effects (depolarization, diattenuation and retardance) [10]. The fundamental form of this matrix is [24, 31]

$$\mathbf{F}^{(0)}(\vec{k}_i, -\vec{k}_i) = \begin{bmatrix} F_{11}^{(0)} & F_{12}^{(0)} & 0 & F_{14}^{(0)} \\ F_{12}^{(0)} & F_{22}^{(0)} & 0 & 0 \\ 0 & 0 & F_{33}^{(0)} & F_{34}^{(0)} \\ F_{14}^{(0)} & 0 & -F_{34}^{(0)} & F_{44}^{(0)} \end{bmatrix}, \quad (4)$$

#179024 - $15.00 USD Received 30 Oct 2012; revised 6 Dec 2012; accepted 6 Dec 2012; published 19 Dec 2012

where the scattering medium is not macroscopically isotropic so the backscattering matrix is a function of the direction of incidence and there are now six degrees of freedom though seven variables are listed in the scattering matrix. This is because reciprocity also imposes the requirement [35]

$$F_{11} - F_{22} + F_{33} - F_{44} = 0. \tag{5}$$

The scattering matrix in Eq. (4) is given the superscript $^{(0)}$ to indicate it is in the scatterer's coordinate basis. In this work we do not assume to know what this basis is. The matrix under interrogation is assumed to be rotated relative to the instrument's polarization basis by some angle φ so that the actual matrix under interrogation is

$$\mathbf{F}(\vec{k}_i, -\vec{k}_i) = \mathbf{R}(\varphi)\mathbf{F}^{(0)}(\vec{k}_i, -\vec{k}_i)\mathbf{R}(\varphi) = \begin{bmatrix} F_{11} & F_{12} & F_{13} & F_{14} \\ F_{12} & F_{22} & F_{23} & F_{24} \\ -F_{13} & -F_{23} & F_{33} & F_{34} \\ F_{14} & F_{24} & -F_{34} & F_{44} \end{bmatrix}, \tag{6}$$

where $\mathbf{R}(\varphi)$ is a rotation matrix of angle φ. The angle φ is measured between the s-polarization in the plane of scatterer orientation and the lidar polarization coordinate basis [10].

2.1. Measuring the scattering matrix

An imperfect polarization lidar may contain depolarizing, diattenuating and retarding effects in $\mathbf{M_{TX}}$ and $\mathbf{M_{RX}}$, non-ideal polarization analyzers, and elliptical laser polarization states with degree of polarization less than one. The scattering volume, however, does not see the behavior of the instrument directly, and we can reduce Eq. (1) to reflect the perspective of $\mathbf{F}$

$$N = \vec{D}^T \mathbf{F}(\vec{k}_i, -\vec{k}_i)\vec{S} \tag{7}$$

where the scattering volume experiences some incident polarization $\vec{S}$, and from the perspective of the scatterer, the lidar instrument measures some polarization $\vec{D}$. The resulting measured signal on the detector, as in Eq. (1), is N. The incident Stokes vector is given from Eq. (1) as

$$\vec{S} = \mathbf{T_{atm}}(\vec{k}_i, R)\mathbf{M_{TX}}\vec{S}_{TX}, \tag{8}$$

and the measured polarization is

$$\vec{D}^T = \vec{o}^T \mathbf{M_{RX}}\mathbf{T_{atm}}(\vec{k}_s, R). \tag{9}$$

where the scalar coefficients in Eq. (1) have been omitted.

The process for measuring a Mueller matrix described by Eq. (7) can be changed to a form that reflects the desire to measure the elements of $\mathbf{F}$. The scattering matrix is rewritten as a vector, $\vec{f}$, of all independent variables with elements [25, 26]

$$f_{i+4(j-1)} = F_{ij} \tag{10}$$

where i and j are indices from one to four and f_k is the kth element of the 1-D vector $\vec{f}$ and F_{ij} is the (i, j) element of the scattering matrix $\mathbf{F}$.

The signal recorded on a detector channel is then given by [25]

$$N = \vec{a}^T \vec{f} \tag{11}$$

where $\vec{a}$ is a measurement vector that is defined by the elements of $\vec{D}$ and $\vec{S}$ in Eq. (7) and is given for a general sixteen element Mueller matrix as

$$a_{i+4(j-1)} = D_i S_j \tag{12}$$

#179024 - $15.00 USD Received 30 Oct 2012; revised 6 Dec 2012; accepted 6 Dec 2012; published 19 Dec 2012

where i and j are indices from one to four, a_k is the kth element of the 1-D vector $\vec{a}$, D_i is the ith element of the measured Stokes vector $\vec{D}$ and S_j is the jth element of the incident Stokes vector $\vec{S}$.

Because the fundamental forms of the scattering matrices have redundant terms, we can further reduce the dimensionality of $\vec{f}$ by eliminating elements where $i > j$. This is reflected in the measurement vector $\vec{a}$ which is then written for the ten elements in Eq. (6) as

$$\vec{a} = \begin{bmatrix} D_1S_1 \\ D_1S_2 + D_2S_1 \\ D_1S_3 - D_3S_1 \\ D_1S_4 + D_4S_1 \\ D_2S_2 \\ D_2S_3 - D_3S_2 \\ D_2S_4 + D_4S_2 \\ D_3S_3 \\ D_3S_4 - D_4S_3 \\ D_4S_4 \end{bmatrix} \tag{13}$$

and now the scattering matrix is described by the vector

$$\vec{f} = \begin{bmatrix} F_{11} & F_{12} & F_{13} & F_{14} & F_{22} & F_{23} & F_{24} & F_{33} & F_{34} & F_{44} \end{bmatrix}^T. \tag{14}$$

In this way the measurements of the medium are adjusted to the expected form of the scattering matrix. In cases where the medium is described by Eq. (3), $\vec{f}$ and $\vec{a}$ are further reduced to have three elements.

When we perform more than one measurement of the scattering matrix, the measurement vectors are consolidated into a matrix [25, 26]

$$\mathbf{A} = \begin{bmatrix} \vec{a}_1^T \\ \vec{a}_2^T \\ \vdots \end{bmatrix}, \tag{15}$$

and the measured signals are a vector

$$\vec{N} = \mathbf{A}\vec{f}. \tag{16}$$

If the system makes multiple linearly independent measurements such that $rank(\mathbf{A}) \geq Dim(\vec{f})$ the scattering matrix can be determined by

$$\vec{f} = \mathbf{A}^{-1}\vec{N}. \tag{17}$$

In cases where $Dim(\vec{N}) > Dim(\vec{f})$, Eq. (17) is over-defined and the inverse operation on $\mathbf{A}$ is replaced with a pseudo-inverse. In this way, additional temporal integration may be achieved in the scattering matrix retrievals.

The uncertainty in this measurement is then given by the covariance matrix of $\vec{f}$ which is related to the statistical uncertainty of the detected vector $\vec{N}$ through [36]

$$\mathbf{\Sigma}_f^2 = \mathbf{A}^{-1}\mathbf{\Sigma}_N^2\left(\mathbf{A}^{-1}\right)^T, \tag{18}$$

where $\mathbf{\Sigma}_x^2$ is the covariance of $\vec{x}$. If the measurement precision of $\vec{N}$ is shot noise limited, its corresponding covariance matrix is diagonal, with the backscatter photon counts (including background) on the diagonals.

#179024 - $15.00 USD Received 30 Oct 2012; revised 6 Dec 2012; accepted 6 Dec 2012; published 19 Dec 2012

The HSRL uses temporally varying measurement matrices to resolve the full backscatter matrix. This technique of substituting temporally changing polarization measurements for simultaneous measurements is not an uncommon lidar technique [33, 37]. Spacing measurements in time means the measured signal will contain both uncertainty from shot noise and atmospheric variability. As a result, the covariance of the measured signals is

$$\mathbf{\Sigma}_N^2 = \mathbf{\Sigma}_{shot}^2 + \mathbf{\Sigma}_{Atm}^2, \tag{19}$$

where $\mathbf{\Sigma}_{shot}^2$ is the covariance matrix of the detected photon counts resulting from shot noise and $\mathbf{\Sigma}_{Atm}^2$ is the covariance of the detected photon counts resulting from variability of atmospheric scattering and extinction terms. This atmospheric term is related to variability of the actual atmospheric scattering matrix, denoted here by a capital subscript F, through the measurement matrix

$$\mathbf{\Sigma}_{Atm}^2 = \mathbf{A}\mathbf{\Sigma}_F^2\mathbf{A}^T. \tag{20}$$

Substituting Eq. (20) into (19) and substituting that result into (18) gives

$$\mathbf{\Sigma}_f^2 = \mathbf{A}^{-1}\mathbf{\Sigma}_{shot}^2\left(\mathbf{A}^{-1}\right)^T + \mathbf{\Sigma}_F^2. \tag{21}$$

Equation (20) and therefore Eq. (21) account for atmospheric variability on time scales greater than or equal to the measurement integration time. For HSRL's 0.5 sec integration time, there is also likely variation at sub-integration time scales. Numerical simulations of HSRL have shown that higher frequency variations result in small covariance terms between between all the scattering matrix elements in $\mathbf{\Sigma}_F^2$. As a result, some zero mean noise is imparted on all scattering matrix elements due to high frequency atmospheric backscatter, extinction and depolarization variability.

Thus, statistical variability of the atmosphere adds uncertainty to the scattering matrix retrieval. It is important to note that it does not bias the measurement in a way that would generate false positive identification of oriented scatterers. We have found, however, that nonlinear detector response, such as pulse pile-up, can bias measurement of off diagonal elements. For this reason, low altitude, high backscatter, water clouds can have false, non-zero off diagonal elements. These false terms generally do not satisfy the criteria for Eq. (5) or the matrix form in Eq. (6). This and our knowledge of the data acquisition system's linear dynamic range make such cases easy to identify.

The polarization formalism shown here provides a simple processing technique for bias free polarization measurements regardless of the lidar's polarization effects. The accuracy of this measurement is limited by the accuracy to which $\vec{D}$ and $\vec{S}$ are known instead of the polarization purity of the system. Imperfections in the measurement such as system retardance, depolarization and diattenuation, non-ideal polarizers and differences in detector gain are folded into $\vec{D}$ and $\vec{S}$ and are fully removed from the scatterer characterization. While we apply this formalism to measuring a full backscatter phase matrix here, it can also be applied to any conventional polarization lidar measurements where optical system effects reduce the accuracy of the measurement.

3. System description

The high spectral resolution lidar at NCAR was designed and built at the University of Wisconsin to directly measure cloud and aerosol backscatter, extinction and circular depolarization [28, 29]. A simplified instrument layout is shown in Fig. 1. The laser is vertically polarized and passes through the transceiver thin film polarizer (TFP). The vertical polarization is then transformed by a quarter wave-plate (QWP) to right hand circular (RHC) polarization. The beam is expanded by an afocal Mersenne Cassegrain telescope. Upon backscattering, the

#179024 - $15.00 USD Received 30 Oct 2012; revised 6 Dec 2012; accepted 6 Dec 2012; published 19 Dec 2012

polarization becomes left hand circular (LHC) due to the change in propagation direction and the QWP transforms this polarization to horizontal. This polarization reflects off the TFP as the parallel channel. Part of parallel polarized signal is picked off by a beam sampler (BS) and passed through an iodine absorption cell to measure the molecular backscatter signal, and the rest passes onto high backscatter (10% port on a beam sampler) and low backscatter (90% port on a beam sampler) parallel polarized total molecular and aerosol detectors (not depicted). The total molecular and aerosol cross polarized signal is picked off behind the TFP with a beam splitter (BS). This signal is then passed to the cross polarized detector. Not shown is an energy monitor in the transmitter that is used to normalize fluctuations in transmitted laser power (less than 5% shot to shot variation).

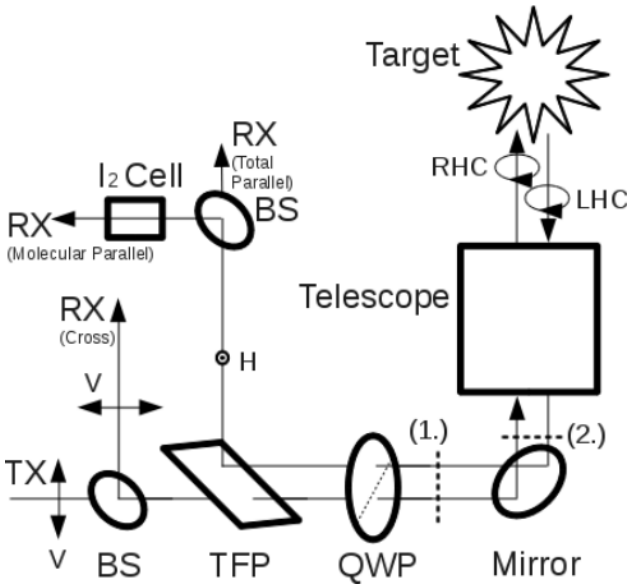

Fig. 1. Layout of HSRL transceiver. The laser is initially vertically polarized and in its original polarization operation, the use of a QWP allows the instrument to measure circular depolarization ratios. By rotating the QWP, the transmitted and detected polarizations actively change, and the rank of the measurement matrix **A** is increased. Additional optics to the left of the QWP such as folding mirrors and polarizers have been omitted. The high backscatter receiver channel has also been omitted.

Some of the NCAR HSRL specifications are listed in Table 1. The narrow field-of-view serves to suppress multiple scattering [38], and even optically thick water clouds have very little depolarization. For this reason, multiple scattering is not likely to be a significant contributer to detected signals.

Table 1. NCAR HSRL Specifications

Wavelength	532 nm	Receiver Field-of-View	100 μrad
Pulse Energy	75 μJ	Beam Divergence	50 μrad
Pulse Rate	4 kHz	Minimum Time Bin	0.5 sec
Receiver Bandwidth	6 GHz	Minimum Altitude Bin	7.5 m

#179024 - $15.00 USD Received 30 Oct 2012; revised 6 Dec 2012; accepted 6 Dec 2012; published 19 Dec 2012

3.1. Modified operation

To measure the full scattering matrix of oriented scatterers we must obtain a measurement matrix of rank greater than ten. Conventional polarization operation only allows for $rank(\mathbf{A}) = 2$. The QWP mount was replaced with a motorized mount to provide more linearly independent polarization measurements. As this QWP rotates, it changes both the transmitted and received polarizations. Both $\vec{D}$ and $\vec{S}$ must change to characterize the full scattering matrix, so systems that do not use a shared telescope configuration would require a rotating wave-plate in both the transmitter and receiver.

The QWP is rotated by a high speed rotation mount with better than 0.1° accuracy of motor rotation angle. This rotation is performed continuously, so the QWP position is not constant over the course of an integrated data point. The measurement vector corresponding to a time integrated data point becomes

$$\vec{a}(\theta) = \int_{\theta}^{\theta+\Delta\theta} \vec{a}_i(\vartheta) d\vartheta, \tag{22}$$

where $\vec{a}_i(\vartheta)$ is the instantaneous measurement vector for the QWP at angle ϑ and $\vec{a}(\theta)$ is the measurement vector with a QWP start angle of θ. The QWP rotation rate is generally set to $74^\circ/sec$.

The data acquisition hardware on the HSRL has a minimum integration time of 0.5 seconds. Thus, 2000 laser shots are recorded over a QWP rotation of 37°. This rotation rate was selected because it minimized the measured depolarization and backscatter uncertainty (uncertainty in other matrix terms were not considered) for all possible QWP angles. The fact that 37 and 360 have no common multiples, forgoes the need to slave the QWP rotation to the HSRL timing unit. Instead, we only record the start and stop position of the QWP for each data point and determine the measurement vector using Eq. (22).

Though only 2.5 seconds of data (5 data points from each channel) are needed to invert Eq. (17), typical scattering matrix calculations use 40 seconds of data per matrix retrieval (80 data points from each channel) to suppress shot noise at altitudes up to 14 km.

To avoid back reflections from the transmitted laser into the receiver, the original HSRL design tilted the QWP in the plane of the optical bread board by approximately 10° relative to the optic axis. As a result, the device is not a true QWP, because the crystal cut designed to produce a $\frac{\pi}{2}$ phase shift between ordinary and extraordinary axes assumes normal incidence. Additionally, the phase shift of the QWP is not constant with rotation angle [39]. Through both modeling [40,41] and experimentation, we have found that the QWP phase shift can be reliably approximated at tilt angles less than 20° as

$$\Gamma(\theta) = \Gamma_0 + \Gamma_1 \cos(\theta - \theta_1) + \Gamma_2 \cos(2\theta), \tag{23}$$

where Γ is the phase shift of the wave-plate, θ is the angle of the QWP fast axis relative to the axis of tilt and Γ_0, Γ_1 and Γ_2 are fundamental, first and second harmonic coefficients for the wave-plate's phase shift. The HSRL uses a quartz compound zero order wave-plate that is tilted by approximately 10°. The coefficient values for this particular configuration are $\Gamma_0 = 1.53$, $\Gamma_1 = 0.09$ and $\Gamma_2 = -1.08$. Theoretically, the phase shift should only have even number harmonics, but wobble in the mount, likely the result of misalignment between the QWP normal and the mount's axis of rotation, contributes the odd first order term. This fact was obvious when characterizing the QWP because the signals were not perfectly 180° periodic with QWP rotation. Note that there is also an offset angle θ_1 indicating that the wobble of the QWP will not necessarily correspond to the QWP fast axis.

The valid range for this approximation generally depends on the wave-plate material, thickness and design. Materials with greater birefringence, thicker wave-plates, and compound zero

#179024 - $15.00 USD Received 30 Oct 2012; revised 6 Dec 2012; accepted 6 Dec 2012; published 19 Dec 2012

order wave-plates generally have a narrower field-of-view and therefore shrink the valid range of Eq. (23).

The value of each term in Eq. (23) was determined by rotating the wave-plate between a horizontal polarizer and an analyzer at 0°, 30°, 60° and 90°. We fit the Fourier coefficients from the recorded signal to Eq. (23) to obtain an initial QWP characterization.

Tilting the QWP has an effect of tilting the trajectory of the QWP's output polarization on the Poincaré sphere (see Fig. 2). Large tilt angles also tend to introduce additional lobes to the path, which are of little benefit, but the expanded lateral coverage from the tilted trajectory improves our ability to resolve angular features, such as the orientation angle φ in Eq. (6).

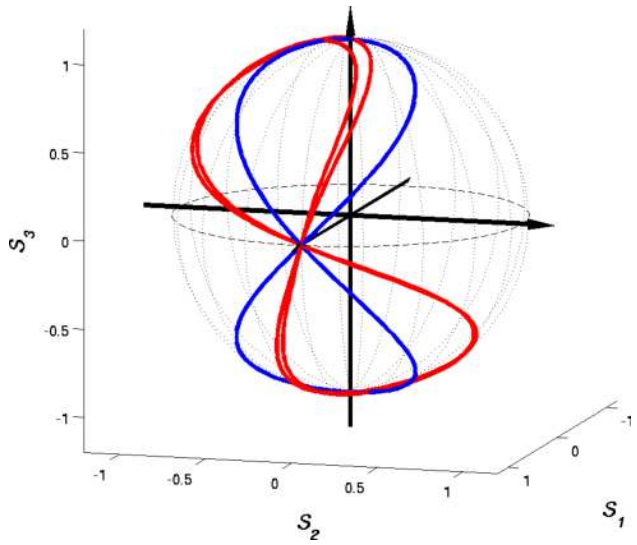

Fig. 2. Poincaré Sphere representation of output polarizations for a horizontally polarized input resulting from an ideal QWP (blue) and the titled QWP (red) used in the HSRL and described in Eq. (23). Tilting the QWP tilts the output polarization trajectory and the first order term results in a path that is not quite periodic for 180° rotation.

In addition to the QWP coefficients in Eq. (23), we also must determine the laser polarized state, the diattenuation vector of all detector channels (total high backscatter, total low backscatter, molecular and cross polarized), and the Mueller matrix of the remaining transmitter optics (folding mirror and a telescope). Each of these terms are known to some reasonable approximation. The laser is designed to be vertically polarized with a high DOP through use of a Glan-Taylor polarizer before the TFP. The total high and low and molecular channels are designed to have horizontal diattenuation vectors with magnitudes near one. Likewise the cross polarized channel is designed to have a vertical diattenuation vector also with magnitude near one. The 45° laser line mirror used to fold the outgoing beam into the telescope was characterized during the lidar modification (diattenuation near zero, phase shift of approximately $\frac{9\pi}{10}$). The low angles of incidence on the cassigrain telescope's mirrors should make the device nearly polarization preserving, but allowances were made for small amounts of depolarization, retardance and diattenuation in the device.

The estimated polarization effects of each of these terms provides the initial conditions for a sequence of optimizations that allows us to determine the measurement vectors of the instrument for any QWP rotation angle. Intensity on each channel is measured as a function of QWP angle in the following setups.

1. A retro-reflection mirror is placed immediately after the QWP at (1.) in Fig. 1.

#179024 - $15.00 USD Received 30 Oct 2012; revised 6 Dec 2012; accepted 6 Dec 2012; published 19 Dec 2012

2. A retro-reflection mirror is placed immediately after the folding mirror at (2.) in Fig. 1.

3. A polarizer, then retro-reflecting mirror are placed immediately after the folding mirror at (2.) in Fig 1. Data is recorded with the polarizer set at 0°, 30° and 60°.

Running a simultaneous Fourier coefficient fit to all the above setups provides the descriptions for all HSRL terms except the telescope. A final fit, including the telescope is performed in the process of data collection off the sky. It is unlikely that any of these polarization terms will change rapidly over time. Thus, the instrument is recharacterized periodically using depolarizing sky returns to guarantee the performance of the instrument. Also, when the HSRL's transmit tilt angle is changed, the only significant change is in the orientation of the folding mirror. The mirror Mueller matrix is rotated by the new tilt angle and the system is characterized using sky returns.

After determining their polarization properties, each channel is well characterized to within a scalar constant. This scalar is the optical efficiency of each channel and must be properly accounted for to use both cross and parallel channels in the full scattering matrix calculation. The HSRL's configuration produces a measurement matrix of rank 15 when both channels are combined and 9 in each individual channel. Typically we use the combination of both polarization channels to determine the volume scattering matrix

$$\vec{f}(R) = \begin{bmatrix} \mathbf{A}_{\parallel} \\ \mathbf{A}_{\perp} \end{bmatrix}^{-1} \begin{bmatrix} \vec{N}_{\parallel}(R) \\ \frac{1}{K(R)}\vec{N}_{\perp}(R) \end{bmatrix}, \tag{24}$$

where $\mathbf{A}_{\parallel}$ and $\mathbf{A}_{\perp}$ represent the measurement matrices of the parallel and cross polarized channels, $\vec{N}_{\parallel}$ and $\vec{N}_{\perp}$ are the detected photon counts on the parallel and cross polarized channels respectively and $K(R)$ is the relative efficiency of the two channels at range R, given by

$$K(R) = \frac{\eta_{\perp} G_{\perp}(R)}{\eta_{\parallel} G_{\parallel}(R)}, \tag{25}$$

where $\eta_{\perp}$ and $G_{\perp}(R)$ are the cross polarized channel efficiency and geometric overlap function respectively and $\eta_{\parallel}$ and $G_{\parallel}(R)$ are the parallel polarized channel efficiency and geometric overlap function respectively.

The value of $K(R)$ can be determined when we can assume only randomly oriented scatterers are present. In that case each channel can independently calculate the reduced scattering matrix of rank three using three or more successive data points.

$$\vec{f}_{\parallel}(R) = \mathbf{A}_{\parallel}^{-1}\vec{N}_{\parallel}(R), \tag{26}$$

$$\vec{f}_{\perp}(R) = \mathbf{A}_{\perp}^{-1}\vec{N}_{\perp}(R). \tag{27}$$

When the polarization of each channel is properly characterized, the resulting phase matrices will only differ by the scalar multiple $K(R)$. Thus, the ratio of the measured backscatter from the two channels provides their relative efficiency

$$K(R) = \frac{F_{11}^{\perp}(R)}{F_{11}^{\parallel}(R)}, \tag{28}$$

This calibration procedure does not require a change in the HSRL operation, and can be performed with any data set where the QWP was rotating.

Figure 3 shows the initially recorded backscatter profiles, $\vec{f}_{\parallel}(R)$ and $\vec{f}_{\perp}(R)$. The perpendicular channel is then corrected by a factor $\frac{1}{K(R)}$ and the resulting profile very nearly agrees with the parallel channel.

#179024 - $15.00 USD Received 30 Oct 2012; revised 6 Dec 2012; accepted 6 Dec 2012; published 19 Dec 2012

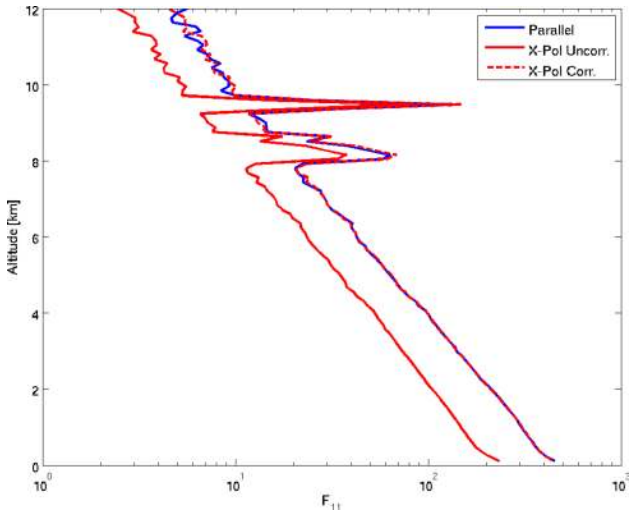

Fig. 3. Measured backscatter, $F_{11}(R)$ on parallel (blue), uncorrected cross polarized (red solid line) and corrected cross polarized (red dashed line) channels. Multiplying the received photon counts on the cross polarized channel by $1/K(R)$ results in retrieval of nearly identical backscatter measurements on the two channels.

Additional scaling and cross talk between the molecular and total channels are covered in [28, 29]. The new polarization operation of the HSRL does not change this calibration except that the individual channel retrievals of the backscatter coefficient (F_{11}) should be used instead of background subtracted photon counts.

With a complete system description we calculate the condition number of the measurement matrix **A** is approximately 25. This relatively high value indicates that the system parameters are not optimized for full scattering matrix retrieval. It may be possible to improve the system performance by further tilting the rotating QWP or replacing it with a custom retarder as suggested by [26]. Slower QWP rotation rates improve the condition of **A**. However, further investigation into uncertainty contributions by atmospheric variability and system time resolution need to be investigated in further detail to perform a proper system optimization. Never-the-less, in its present configuration, the HSRL is able to retrieve the full backscatter matrix of oriented scatterers.

4. Observations

The NCAR HSRL began collecting full backscatter phase matrix data over Boulder, CO, USA starting in May 2012. On July 16, 2012 at 2PM local time (1600 UT), the lidar was tilted 20° off zenith when a heavy rain storm passed over. During this time the cloud overhead was ice or mixed phase. The time resolved backscatter ratio, depolarization and diattenuation of the event are shown in Fig. 4. Note the use of a single depolarization term to describe the oriented rain is not technically correct, but the product is shown to provide a conventional lidar context for oriented scatterer observations. We presently use diattenuation defined as $\frac{F_{12}^{(0)}}{F_{11}^{(0)}}$ to identify the presence of oriented scatterers. The time integrated backscatter phase matrix profile is shown in Fig. 5. The cloud above 2.5 km is strictly depolarizing where there are no off diagonal terms in the cloud scattering matrix. However, the altitudes where rain is present have significant off diagonal terms due to the preferential orientation of the larger raindrops. This profile shows that

#179024 - $15.00 USD Received 30 Oct 2012; revised 6 Dec 2012; accepted 6 Dec 2012; published 19 Dec 2012

the instrument is able to characterize oriented and randomly oriented scatterers within the same profile.

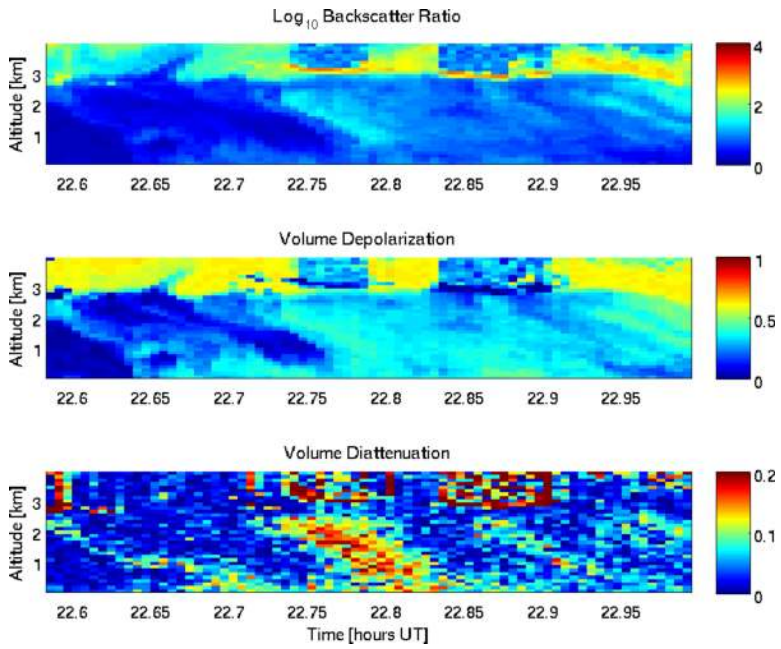

Fig. 4. Backscatter ratio (top), depolarization (middle) and diattenuation (bottom) of a rain storm containing oriented rain drops observed on July 16, 2012. The areas of large diattenuation suggest the presence of large raindrops.

In another observation on July 2, 2012 at 5AM local time (1100 UT), the HSRL was operating at a 30° tilt angle when an ice cloud passed over at approximately 5 km. Horizontally oriented ice crystals were present. Fig. 6 shows the time resolved backscatter ratio depolarization and diattenuation of the ice cloud. Again the use of depolarization where ice crystals are oriented is not technically correct, but the profile shows that the randomly oriented volumes, and therefore by extension oriented volumes, are composed of ice. The observed cloud consists entirely of ice, but preferential orientation, indicated by the diattenuation profile, only exists in a relatively narrow altitude range. There is also some temporal variability in the orientation. It is not clear if this is because of a change in the ice crystal characteristics, advection or other environmental conditions that might disrupt the crystal orientation behavior (such as turbulence).

Fig. 7 shows the time integrated scattering matrix parameters of the oriented ice cloud from Fig. 6. Off diagonal terms in the matrix are non-zero only within a narrow altitude band of between 5 and 5.5 km. Note also that where oriented ice crystals are present, the magnitudes of diagonal terms F_{22}, F_{33} and F_{44} are larger than the rest of the randomly oriented cloud. The depolarizing effect where the oriented ice crystals are present is less than that of fully randomly oriented volumes. Depolarization is often an indicator of randomness within the volume. The fact that the depolarization does not become zero may be the result of ice crystal properties (such as roughness), broad size distributions or a significant randomly oriented sub-population.

#179024 - $15.00 USD Received 30 Oct 2012; revised 6 Dec 2012; accepted 6 Dec 2012; published 19 Dec 2012

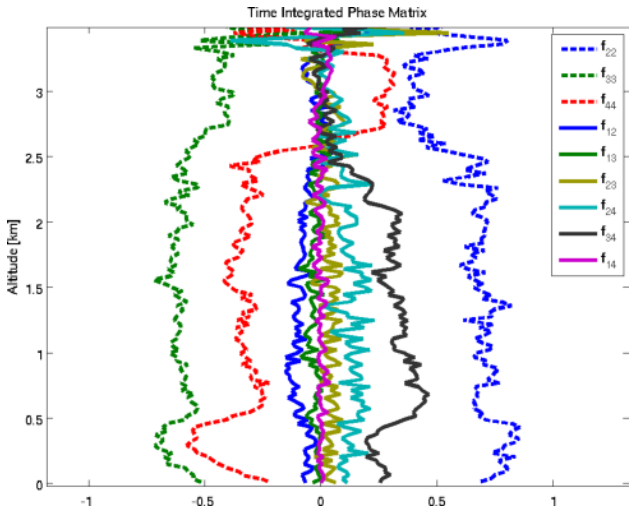

Fig. 5. Observed normalized backscatter phase (Mueller) matrix of heavy rainfall with a mixed phase cloud above it. The profile is time integrated over the highly diattenuating rain in Fig. 4. Diagonal matrix terms are dashed and off diagonals are solid. The cloud above 2.5 km is strictly depolarizing (randomly oriented) with off diagonal terms all zero. The rain below 2.5 km consists of oriented oblate spheroids which have a common preferred orientation.

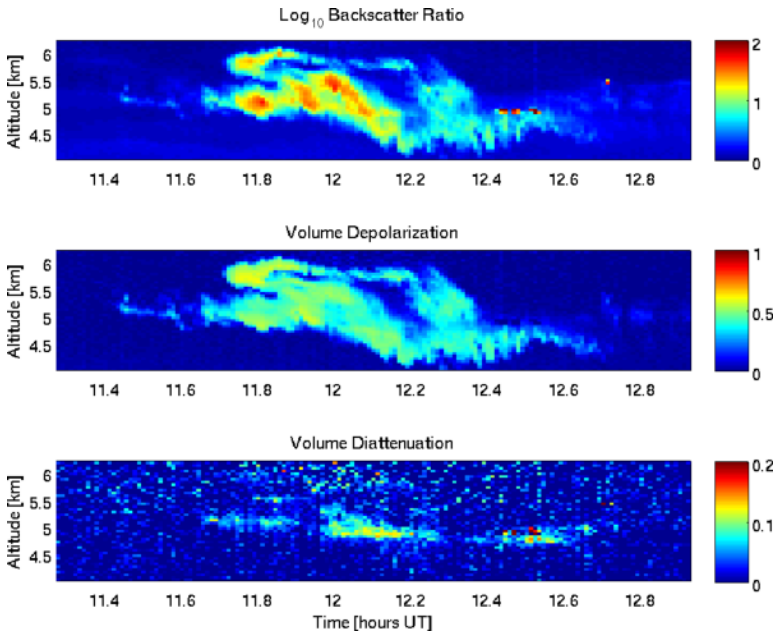

Fig. 6. Backscatter ratio (top), depolarization (middle) and diattenuation (bottom) of an ice cloud containing oriented ice crystals observed on July 2, 2012. The presence of the oriented ice crystals is not clear from the backscatter and depolarization profiles alone, but non-zero diattenuation indicates preferential orientation occurring mostly in an altitude band near 5 km..

#179024 - $15.00 USD Received 30 Oct 2012; revised 6 Dec 2012; accepted 6 Dec 2012; published 19 Dec 2012

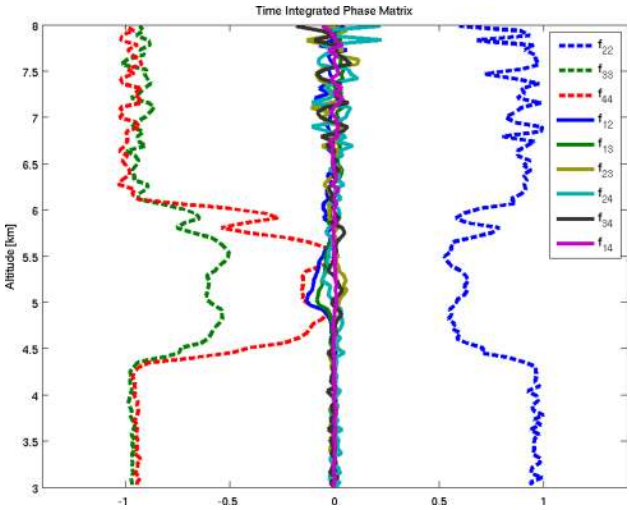

Fig. 7. Observed normalized backscatter phase (Mueller) matrix of ice cloud with a thin layer of oriented ice crystals. Diagonal matrix terms are dashed and off diagonal are solid. Most of the profile is strictly depolarizing, but there is a narrow (approximately 0.5 km) altitude range starting at 5 km that contains non-zero off diagonal scattering terms, indicating the presence of oriented ice crystals.

5. Conclusion

We have demonstrated that the capability to measure the full backscatter phase matrix can be integrated into a lidar instrument through a relatively simple hardware modification. The processing of the instrument's data requires some basic matrix operations to retrieve the full backscatter phase matrix. Unlike conventional polarization lidar data products, this quantity is unambiguous when oriented scatterers are present and in such cases provides additional polarization data that may be used to improve the accuracy of scattering inversions.

In performing these modifications to NCAR's HSRL, we demonstrate that the measurement can be performed on an instrument with significant polarization effects. The modification did not sacrifice the already existing capabilities of the instrument and further improved our ability to calibrate the two polarization channels.

While polarization lidar measurements of the atmosphere have been made for decades, there are very few experimental studies demonstrating specific values of backscatter phase matrices. The significance of oriented ice crystals for remote sensing inversions and radiative transfer inevitably depends on these scattering terms. Through this expanded polarization capability, NCAR's HSRL will begin to further develop the relationship between orientation and polarization and other physical parameters of the atmosphere.

#179024 - $15.00 USD Received 30 Oct 2012; revised 6 Dec 2012; accepted 6 Dec 2012; published 19 Dec 2012